International Journal of Heat and Fluid Flow 30 (2009) 481–493

Contents lists available at ScienceDirect

International Journal of Heat and Fluid Flow

journal homepage: www.elsevier.com/locate/ijhff

Numerical investigation of a perturbed swirling annular two-phase jet

George A. Siamas *, Xi Jiang, Luiz C. Wrobel

Mechanical Engineering, School of Engineering and Design, Brunel University, Uxbridge UB8 3PH, UK

ARTICLE INFO

Article history:
Received 12 September 2008
Received in revised form 13 February 2009
Accepted 16 February 2009
Available online 8 April 2009

Keywords:
Direct numerical simulation
Two-phase
Jet
Swirl
Perturbation
Annular

ABSTRACT

A swirling annular gas–liquid two-phase jet flow system has been investigated by solving the compressible, time-dependent, non-dimensional Navier–Stokes equations using highly accurate numerical methods. The mathematical formulation for the flow system is based on an Eulerian approach with mixed-fluid treatment while an adjusted volume of fluid method is utilised to account for the gas compressibility. Surface tension effects are captured by a continuum surface force model. Swirling motion is applied at the inlet while a small helical perturbation is also applied to initiate the instability. Three-dimensional spatial direct numerical simulation has been performed with parallelisation of the code based on domain decomposition. The results show that the flow is characterised by a geometrical recirculation zone adjacent to the nozzle exit and by a central recirculation zone further downstream. Swirl enhances the flow instability and vorticity and promotes liquid dispersion in the cross-streamwise directions. A dynamic precessing vortex core is developed demonstrating that the growth of such a vortex in annular configurations can be initiated even at low swirl numbers, in agreement with experimental findings. Analysis of the averaged results revealed the existence of a geometrical recirculation zone and a swirl induced central recirculation zone in the flow field.

1. Introduction

Gas–liquid two-phase flow systems are encountered in a variety of engineering applications such as sprays in fuel injection in combustion engines and in propulsion systems (Gorokhovski and Herrmann, 2008). A liquid sheet spray process is a two-phase flow system with a gas, in most cases air, as the continuous phase and a liquid as the dispersed phase in the form of droplets of ligaments. In most applications the gas phase is a high-speed compressible flow while the liquid exhibits natural incompressibility. The two phases are coupled through exchange of mass, momentum and energy with their interactions occurring in different ways at various time scales. Understanding of the fluid dynamic behaviour of liquid sheets in gas medium is essential to achieve effective control of the desired transfer rates of the two-phase flow system.

Compared with round jets annular jets are advantageous in many applications due to the existence of thin liquid sheets, which can disintegrate faster, leading to more effective atomisation. However, the annular configuration results in more complex flow fields compared to round configurations due to the existence of two concentric shear layers near recirculation zone immediately after the nozzle exit (Siamas et al., 2008a; Del Taglia et al., 2004; Sheen et al., 1996), which is a typical feature of annular jet flows.

The addition of swirling motion in annular jet flows, found in propulsion systems and other combustion systems, is regarded as an effective way to stabilise the flame near the burner exit (Gupta et al., 1984). Higher entrainment and improved flow mixing in the shear-layer region can be achieved by the introduction of swirl (Hübner et al., 2003; Sheen et al., 1996). The addition of swirl in atomisation systems can also significantly alter the spray physics and speed-up the liquid disintegration process (Liao et al., 2000). It is very difficult to understand the physics behind liquid breakup and atomisation using theoretical and/or experimental approaches due to the complex mixing and coupling between the liquid and the gas phases and the broad range of time and length scales involved. The existing studies on annular jets were mainly based on experimental observations (Vanierschot and van den Bulck, 2007; Adzic et al., 2001; Ramamurthi and Tharakan, 1998; Sommerfeld and Qiu, 1991) and on simple mathematical formulations (Ibrahim and McKinney, 2006; Liao et al., 2000; Chuech, 1993). There is still a lack of fundamental understanding on the fluid dynamic behaviour of swirling annular gas–liquid two-phase jets.

Detailed understanding of the fluid behaviour of complex two-phase flow systems requires temporally and spatially resolved diagnostics. In terms of obtaining elementary understanding, DNS is advantageous over the traditional Reynolds-averaged Navier–Stokes (RANS) modelling approach and the more advanced large-eddy simulation (LES). The addition of swirl causes extra problems since the swirling motion cannot be easily modelled using RANS due to effects of the mean flow streamline curvature

* Corresponding author. Tel.: +357 25 723852; fax: +357 25 722366.
E-mail addresses: siamas@spidernet.com.cy, george.siamas@brunel.ac.uk (G.A. Siamas).

0142-727X/$ - see front matter © 2009 Published by Elsevier Inc.
doi:10.1016/j.ijheatfluidflow.2009.02.020

Nomenclature

A	amplitude of disturbance
a_1, a_2	storage locations constants
D	mass diffusivity
e	internal energy per unit mass
E_T	total energy of the gas $\rho_g[e+(u^2+v^2+w^2)/2$
f_0	excitation frequency
f_x, f_θ	swirl constants
j	grid point j
L	length
Ma	Mach number
m	mode number
Pr	Prandtl number
P	gas pressure
Q	solution variables
Q_1, Q_2	storage locations
q	heat flux
R	radius
Re	Reynolds number
Re_t	turbulent Reynolds number
r	radial distance
S	swirl number
Sc	Schmidt number
T	temperature
t	time
$\boldsymbol{U}$, $\boldsymbol{E}$, $\boldsymbol{F}$, $\boldsymbol{G}$, $\boldsymbol{H}$	vectors
u, v, w	velocity components in x, y, z directions
u_θ	azimuthal velocity
We	Weber number
x, y, z	Cartesian coordinates
Y	liquid mass fraction

Greek symbols

γ	ratio of specific heats of gas
η_K	Kolmogorov length scale
η_{grid}	grid spacing
κ	curvature
μ	viscosity
ρ	density
σ	surface tension
τ	viscous stress
Φ	liquid volume fraction
ϕ	azimuthal angle
ϕ_j	general variable

Subscripts

a	ambient
g	gas
i, o	inner and outer radii of the annular jet
l	liquid
ref	reference
zs	sponge layer

Superscripts

*	dimensional quantity
$'$, $''$	first and second derivatives

Other symbols

Δ	difference operator
∇	gradient
$-$	mean or time-average
$\|\|$	modulus

(Jakirlic et al., 2002). LES can be utilised to overcome the problems associated with RANS approach but it may not be sufficient to understand the detailed mechanisms in high-speed gas–liquid two-phase jet flow, as the small scales still need to be modelled in LES. The swirling motion can be captured using LES but only the major part of the turbulent motion is directly resolved (Garcia-Villalba et al., 2006; Garcia-Villalba and Frohlich, 2006). From this perspective DNS can be very useful in increasing understanding of complex multiphase flows and provide useful databases for the development of atomisation models.

Ruith and Meiburg (2002), Kollmann et al. (2001) used DNS to simulate vortex breakdown in single-phase swirling jets, but DNS of two-phase flows has been extremely scarce. The interface changes and turbulence in two-phase environments have been simulated using DNS (Banerjee et al., 2004; Fulgosi et al., 2003; Lombardi et al., 1996) but the two phases were divided into two single-phase subdomains while the gas flow was considered to be incompressible. Klein (2005) performed DNS of a liquid sheet exhausting into a gaseous incompressible atmosphere under moderate Reynolds number. Direct computations of two-phase gas–liquid flows have been performed in axisymmetric and planar configurations (Siamas et al., 2008a; Siamas and Jiang, 2007; Jiang and Siamas, 2007) and good agreement with linear theories has been obtained. However, the capturing of the fine details of the liquid topology and vortex interaction was not possible in idealised axisymmetric and planar simulations due to the lack of three-dimensional (3D) vortex stretching and interaction. Furthermore, it was not possible to examine swirling flows in axisymmetric or planar simulations. Extended study in full three-dimensions is needed for detailed realisation of the dynamics of annular gas–liquid two-phase swirling jet flow. Recently, an effort has been made by Siamas et al. (2008b) to perform a fully 3D parallel DNS of an annular gas–liquid two-phase jet flow, but it was limited to a non-swirling jet only.

This is an extended effort of the previous study (Siamas et al., 2008b), aiming at a better understanding of annular gas–liquid two-phase jet flows under swirling conditions. The flow physics is examined by direct solution of the unsteady, non-dimensional Navier–Stokes equations using highly accurate numerical methods for the gas–liquid two-phase flow system with gas treated as compressible. Fully 3D parallel spatial direct numerical simulation (DNS) has been performed. In the following sections, governing equations and numerical methods used are presented, followed by discussions on the results and the conclusions drawn.

2. Governing equations

For the swirling annular gas–liquid two-phase jet under investigation, the flow field concerned is the region above the jet nozzle plane where the two-phase jet is issuing into an ambient environment. The flow field is described by the non-dimensional time-dependent Navier–Stokes equations in the Cartesian coordinate system (x,y,z), where the z-axis is aligned with the streamwise direction of the jet while the x–y plane is the cross-stream direction. Reference quantities used in the normalisation are the maximum streamwise velocity at the jet nozzle exit (computational domain inlet), the diameter of the annular jet (twice of the distance between the middle point of the annular sheet and the geometrical centre of the jet nozzle exit), the ambient temperature, gas density and viscosity and the liquid surface tension (assumed to be constant, resulting in a non-dimensional value of one). In the Eulerian

approach with mixed-fluid treatment adopted (Crowe, 2006), the two phases are assumed to be in local kinetic and thermal equilibrium, i.e. the relative velocities and temperatures are not significant, while the density and viscosity are considered as gas–liquid mixture properties. The liquid is assumed to be a passive scalar that is transported by the gas phase. In the current formulation only a non-reacting isothermal flow is considered, where the two phases exchange momentum only without phase change and energy transfer taking place. Thus $u_g = u_l = u$, $v_g = v_l = v$, $w_g = w_l = w$ and $T_g = T_l = T$. The Eulerian approach with mixed-fluid treatment significantly reduces the computational costs due to its simplicity. The drawback of the mixed-fluid treatment is that it is not able to model multiphase flows with the existence of sharp interfacial gradients. These drawbacks may be overcome by the use of a separated-fluid approach (Crowe, 2006) but currently the computational cost is extremely prohibitive. It is worth pointing out that the formulation used herein applies only to situations where the liquid represents a dilute phase such as liquid sheets in an annular configuration. The governing equations are formulated upon the conservation laws for mass, momentum and energy and they describe both phases in a single set of equations. Using the variables defined in the Notation, the non-dimensional governing equations can be written in vector form as

$$\frac{\partial \boldsymbol{U}}{\partial t}+\frac{\partial \boldsymbol{E}}{\partial x}+\frac{\partial \boldsymbol{F}}{\partial y}+\frac{\partial \boldsymbol{G}}{\partial z}+\boldsymbol{H}=0, \tag{1}$$

where the vectors $\boldsymbol{U}$, $\boldsymbol{E}$, $\boldsymbol{F}$, $\boldsymbol{G}$ and $\boldsymbol{H}$ are defined as

$$\boldsymbol{U}=\begin{pmatrix}\rho_g\\ \rho u\\ \rho v\\ \rho w\\ E_r\\ \rho Y\end{pmatrix},\quad \boldsymbol{E}=\begin{bmatrix}\rho_g u\\ \rho u^2+p-\tau_{xx}\\ \rho uv-\tau_{xy}\\ \rho uw-\tau_{xz}\\ (E_T+p)u+q_x-u\tau_{xx,g}-v\tau_{xy,g}-w\tau_{xz,g}\\ \rho uY-\frac{1}{ReSc}\left(\mu\frac{\partial Y}{\partial x}\right)\end{bmatrix},$$

$$\boldsymbol{F}=\begin{bmatrix}\rho_g v\\ \rho uv-\tau_{xy}\\ \rho v^2+p-\tau_{yy}\\ \rho uw-\tau_{yz}\\ (E_T+p)v+q_y-u\tau_{xy,g}-v\tau_{yy,g}-w\tau_{yz,g}\\ \rho vY-\frac{1}{ReSc}\left(\mu\frac{\partial Y}{\partial y}\right)\end{bmatrix},$$

$$\boldsymbol{G}=\begin{bmatrix}\rho_g w\\ \rho uw-\tau_{xz}\\ \rho vw-\tau_{yz}\\ \rho w^2+p-\tau_{zz}\\ (E_T+p)w+q_z-u\tau_{xy,g}-v\tau_{yz,g}-w\tau_{zz,g}\\ \rho wY-\frac{1}{ReSc}\left(\mu\frac{\partial Y}{\partial z}\right)\end{bmatrix},\quad \boldsymbol{H}=\begin{pmatrix}0\\ -\frac{\sigma\kappa}{We}\frac{\partial \Phi}{\partial x}\\ -\frac{\sigma\kappa}{We}\frac{\partial \Phi}{\partial y}\\ -\frac{\sigma\kappa}{We}\frac{\partial \Phi}{\partial z}\\ 0\\ 0\end{pmatrix}. \tag{2}$$

In the governing equations, gravitational terms were not considered due to the relatively high-speed of the jet and the thin distribution of the liquid sheet. The constitutive relations for viscous stress and heat flux components are given in Table 1. Assuming the gas medium as an ideal gas, the governing equations for the gas–liquid two-phase flow system include also the perfect gas law, given by

$$p=\frac{\rho_g T}{\gamma Ma^2}. \tag{3}$$

The physics of the gas–liquid interface are computed and analysed using the volume of fluid (VOF) method by Hirt and Nichols (1981), which employs the liquid volume fraction. The liquid volume fraction works as an indicator to identify the different fluids. A liquid volume fraction value of one, $\Phi = 1$, corresponds to pure liquid and a value of zero, $\Phi = 0$, corresponds to pure gas. In between

Table 1
The constitutive relations for viscous stress and heat flux components.

Gas–liquid mixture	Gas
$\tau_{xx}=-\frac{2}{3}\frac{\mu}{Re}\left(-2\frac{\partial u}{\partial x}+\frac{\partial v}{\partial y}+\frac{\partial w}{\partial z}\right)$	$\tau_{xx,g}=-\frac{2}{3}\frac{\mu_g}{Re}\left(-2\frac{\partial u}{\partial x}+\frac{\partial v}{\partial y}+\frac{\partial w}{\partial z}\right)$
$\tau_{xy}=\frac{\mu}{Re}\left(\frac{\partial v}{\partial x}+\frac{\partial u}{\partial y}\right)$	$\tau_{xy,g}=\frac{\mu_g}{Re}\left(\frac{\partial v}{\partial x}+\frac{\partial u}{\partial y}\right)$
$\tau_{xz}=\frac{\mu}{Re}\left(\frac{\partial w}{\partial x}+\frac{\partial u}{\partial z}\right)$	$\tau_{xz,g}=\frac{\mu_g}{Re}\left(\frac{\partial w}{\partial x}+\frac{\partial u}{\partial z}\right)$
$\tau_{yy}=-\frac{2}{3}\frac{\mu}{Re}\left(\frac{\partial u}{\partial x}-2\frac{\partial v}{\partial y}+\frac{\partial w}{\partial z}\right)$	$\tau_{yy,g}=-\frac{2}{3}\frac{\mu_g}{Re}\left(\frac{\partial u}{\partial x}-2\frac{\partial v}{\partial y}+\frac{\partial w}{\partial z}\right)$
$\tau_{yz}=\frac{\mu}{Re}\left(\frac{\partial w}{\partial y}+\frac{\partial v}{\partial z}\right)$	$\tau_{yz,g}=\frac{\mu_g}{Re}\left(\frac{\partial w}{\partial y}+\frac{\partial v}{\partial z}\right)$
$\tau_{zz}=-\frac{2}{3}\frac{\mu}{Re}\left(\frac{\partial u}{\partial x}+\frac{\partial v}{\partial y}-2\frac{\partial w}{\partial z}\right)$	$\tau_{zz,g}=-\frac{2}{3}\frac{\mu_g}{Re}\left(\frac{\partial u}{\partial x}+\frac{\partial v}{\partial y}-2\frac{\partial w}{\partial z}\right)$
	$q_x=\frac{-\mu}{(\gamma-1)Ma^2PrRe}\frac{\partial T}{\partial x}$
	$q_y=\frac{-\mu}{(\gamma-1)Ma^2PrRe}\frac{\partial T}{\partial y}$
	$q_z=\frac{-\mu}{(\gamma-1)Ma^2PrRe}\frac{\partial T}{\partial z}$

the two values, $0 < \Phi < 1$, a gas–liquid interface region exists and the fluid is considered as a mixture. In this study, the original VOF method has been adapted to solve an equation for the liquid mass fraction γ rather than the volume fraction Φ in order to suit the compressible gas phase formulation (Siamas et al., 2008a; Siamas and Jiang, 2007; Jiang and Siamas, 2007). From their definitions, a relation between liquid volume fraction and liquid mass fraction can be derived as

$$\Phi=\frac{\rho_g Y}{\rho_l-(\rho_l-\rho_g)Y}. \tag{4}$$

Following Gueyffier et al. (1999), the density and viscosity of the gas–liquid two-phase fluid flow are considered as functions of the liquid volume fraction and densities and viscosities of both phases, given by

$$\rho=\Phi\rho_l+(1-\Phi)\rho_g, \tag{5}$$

$$\mu=\Phi\mu_l+(1-\Phi)\mu_g. \tag{6}$$

Eqs. (5) and (6) are utilised in conjunction with the VOF method, to account for the contributions of the two individual phases to the mixture properties.

The gas–liquid interface dynamics are resolved using a continuum surface force (CSF) model developed by Brackbill et al. (1992), which represents the surface tension effect as a continuous volumetric force acting within the region where the two phases coexist. The CSF model overcomes the problem of directly computing the surface tension integral that appears in the Navier–Stokes momentum equations, which requires the exact shape and location of the interface. In the CSF model, the surface tension force in its non-dimensional form, as it appears in Eq. (2), can be approximated as $\sigma\kappa/We\nabla\Phi$, with the curvature of the interface given by

$$\kappa=-\nabla\cdot\left(\frac{\nabla\Phi}{|\nabla\Phi|}\right). \tag{7}$$

3. Computational procedures

3.1. Numerical schemes and parallelisation

The numerical methods include the high-order finite-difference schemes for time advancement and spatial discretisation. The governing equations are integrated forward in time using a third-order compact-storage fully explicit Runge–Kutta scheme (Williamson, 1980). The solution variables $(\rho_g, \rho u, \rho v, \rho w, E_T, \rho Y)$ in Eq. (2) are advanced in time using a three-step compact-storage third-order Runge–Kutta scheme of the family derived by Wray (1986). Two storage locations are employed for each time-dependent variable and at each sub-step at these locations, say Q_1 and Q_2 with Q representing the solution variables, are updated simultaneously as follows:

$$Q_1^{new}=a_1Q_1^{old}\Delta t+Q_2^{old},\quad Q_2^{new}=a_2Q_1^{old}\Delta t+Q_2^{old}. \tag{8}$$

The constants (a_1, a_2) in Eq. (8) are chosen to be (2/3,1/4) for sub-step 1, (5/12,3/20) for sub-step 2 and (3/5,3/5) for sub-step 3. At the beginning of each full time step, Q_1 and Q_2 are equal. The data in Q_1 is used to compute $\partial \boldsymbol{U}/\partial t$ in Eq. (1). The computed $\partial \boldsymbol{U}/\partial t$ is stored in Q_1 to save storage (overwriting the old Q_1). Eq. (8) is then used to update Q_1 and Q_2. In Eq. (8), Δt is the time step, which is limited by the Courant–Friedrichs–Lewy (CFL) condition for stability.

During the time advancement, the density and viscosity of the gas–liquid two-phase flow system are calculated according to Eqs. (5) and (6), using the volume fraction Φ calculated from Eq. (4). However, the liquid mass fraction Y in Eq. (4) needs to be calculated from the solution variable ρY first. Using q to represent ρY at each time step, the liquid mass fraction Y can be calculated as

$$Y = \frac{\rho_1 q}{\rho_l \rho_g + (\rho_l - \rho_g) q}. \tag{9}$$

Eq. (9) can be derived from Eqs. (4), (5). At each time step, Eq. (9) is used first to calculate the liquid mass fraction, Eq. (4) is then used to calculate the liquid volume fraction and Eqs. (5) and (6) are finally used to update the mixture density and viscosity.

Spatial differentiation is achieved using the sixth-order compact (*Padé*) finite-difference scheme of Lele (1992), which has been widely used in DNS of fluid flow problems. The scheme is of sixth-order at the inner points, of fourth-order at the next to the boundary points and of third-order at the boundary. For a general variable ϕ_j at grid point j in the y-direction, the scheme can be written in the following form for the first and second derivatives:

$$\phi'_{j-1} + 3\phi'_j + \phi'_{j+1} = \frac{7}{3}\frac{\phi_{j+1} - \phi_{j-1}}{\Delta y} + \frac{1}{12}\frac{\phi_{j+2} - \phi_{j-2}}{\Delta y}, \tag{10}$$

$$\phi''_{j-1} + \frac{11}{2}\phi''_j + \phi''_{j+1} = 6\frac{\phi_{j+1} - 2\phi_j + \phi_{j-1}}{\Delta y^2} + \frac{3}{8}\frac{\phi_{j+2} - 2\phi_j + \phi_{j-2}}{\Delta y^2}, \tag{11}$$

where Δy is the grid distance in the y-direction. The left hand side of Eqs. (10) and (11) leads to a tridiagonal system of equations whose solutions are obtained by solving the system using a tridiagonal matrix algorithm.

To perform parallel computations, the entire physical domain is divided into "vertical" and "horizontal" slices using domain decomposition method, as shown in Fig. 1. The use of these slices enables correct calculation of the derivatives in all three directions. The "horizontal" slices are used to calculate the x- and y-derivatives while the "vertical" slices are used to calculate the z-derivatives. To enable calculations in three-dimensions the flow data are interlinked by swapping the flow variables from the x–z planes to the x–y planes and vice versa. An intermediate array was used to facilitate the variables for swapping the data between the "vertical" and "horizontal" subdomains. Data exchange amongst the utilised processors is achieved through standard Message Passing Interface (MPI).

3.2. Boundary conditions

The 3D computational domain is bounded by the inflow and the outflow boundaries in the streamwise direction and open boundaries with the ambient field in the jet radial (cross-streamwise) direction. The non-reflecting characteristic boundary conditions due to Thompson (1987) are applied at the open boundaries, which prevent the wave reflections from the outside of the computational domain. The non-reflecting boundary conditions are also used at the outflow boundary in the streamwise direction. The spurious

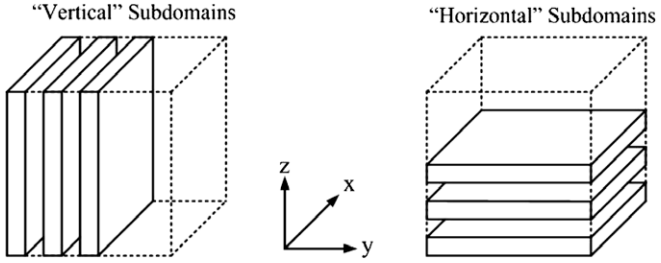

Fig. 1. Schematic of the parallelised computational domain with "vertical" and "horizontal" slices.

wave reflections from outside the boundary have been further controlled by using a sponge layer ($L_{zs} < z < L_z$) next to the outflow boundary (Jiang and Luo, 2000), which has been proved to be very effective in controlling the wave reflections through the outflow boundary. The results of the sponge layer are unphysical and therefore are not used in the data analysis.

The inflow conditions at the jet nozzle exit need careful attention. They represent the initial mass and momentum distributions of the annular gas–liquid two-phase jet. Under swirling conditions, they must be able to represent the amount of swirl at the jet nozzle exit as realistically as possible. Based on the concept of Pierce and Moin (1998) for numerical generation of equilibrium swirling inflow conditions, analytical solutions of the axial and azimuthal velocity components were derived, which enable simple and pre-

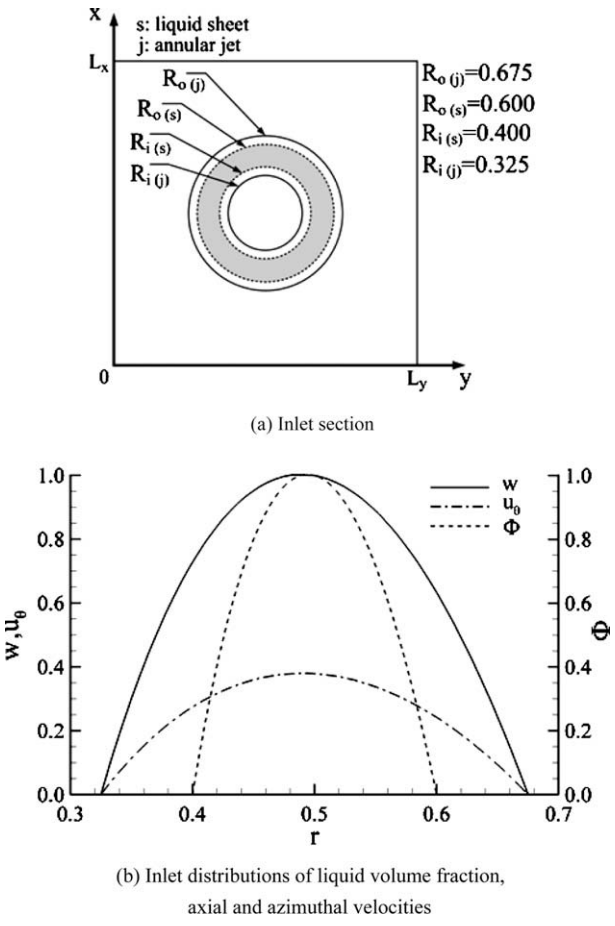

Fig. 2. Schematic of the inlet section and inlet distributions of liquid volume fraction, axial and azimuthal velocities.

cise definition of the desired swirl level (Jiang et al., 2008). The analytical profiles of axial and azimuthal velocities are given as

$$w = -\frac{1}{4}\frac{f_x}{\mu}\left(r^2 - \frac{R_i^2 - R_o^2}{\ln R_i - \ln R_o}\ln r + \frac{R_i^2 \ln R_o - R_o^2 \ln R_i}{\ln R_i - \ln R_o}\right),$$
$$u_\theta = -\frac{1}{3}\frac{f_\theta}{\mu}\left(r^2 - \frac{R_i^2 + R_i R_o + R_o^2}{R_i + R_o}r + \frac{R_i^2 R_o^2}{R_i + R_o}\frac{1}{r}\right), \quad (12)$$

where $r = \sqrt{(x - x_0)^2 + (y - y_0)^2}$ is the radial distance with (x_0, y_0) representing the location of the geometrical centre of the jet nozzle exit, R_i and R_o are the inner and outer radii of the annular jet respectively. In Eq. (12) f_x and f_θ can be defined by the maximum velocities at the inflow boundary. For a unit maximum velocity, which is often the case when a non-dimensional form of the governing equations is employed, the constant f_x is defined as

$$f_x = -\frac{8\mu(\ln R_o - \ln R_i)}{R_o^2 - R_i^2 + R_i^2 \ln\left[\frac{R_i^2 - R_o^2}{2(\ln R_i - \ln R_o)}\right] - R_o^2 \ln\left[\frac{R_i^2 - R_o^2}{2(\ln R_i - \ln R_o)}\right] - 2R_i^2 \ln R_o + 2R_o^2 \ln R_i}. \quad (13)$$

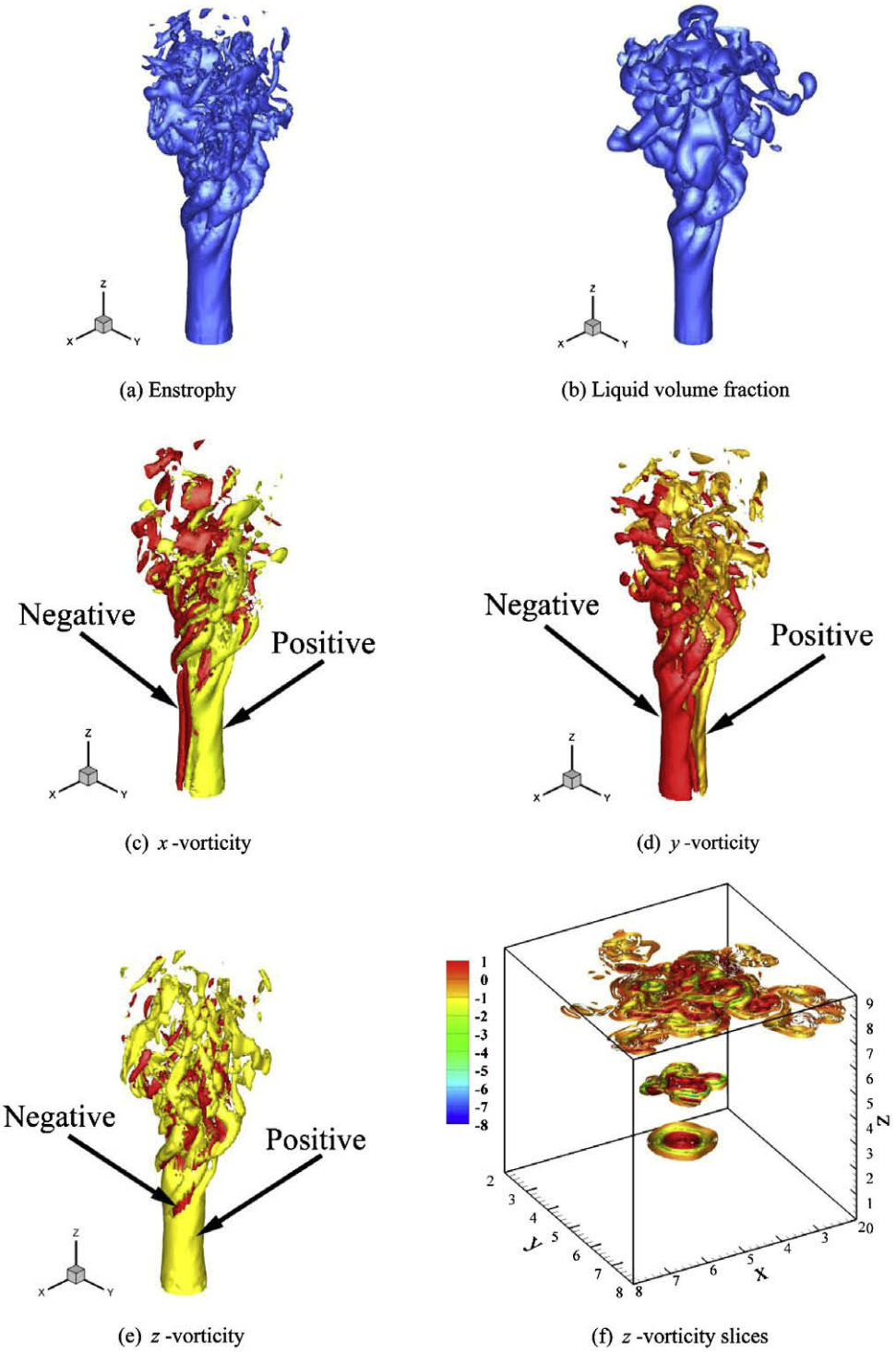

Fig. 3. Instantaneous isosurfaces of enstrophy, liquid volume fraction and the vorticity components at $t = 30.0$.

The parameter f_θ defines the degree of swirl. For known w and u_θ the swirl number can be calculated from

$$S = \frac{\int_{R_i}^{R_o} w u_\theta r^2 dr}{R_o \int_{R_i}^{R_o} w^2 r dr}. \quad (14)$$

A certain swirl number can be conveniently achieved by adjusting the constant f_θ in Eq. (12). From the azimuthal velocity u_θ, the cross-streamwise velocity components at the inflow can be specified by $u = -u_\theta y/r$ and $v = u_\theta x/r$. At the inflow boundary, the liquid mass fraction profile has been specified using a distribution similar to the streamwise (axial) velocity profile. The inlet profiles of liquid volume fraction, axial and azimuthal velocities, along with a schematic of the inlet section are shown in Fig. 2.

The mean velocity at the inflow was perturbed by a flapping mode that contains two helical modes with the same frequency and amplitude (Uchiyama, 2004). The velocity components at the jet nozzle exit $z = 0$ can be given as

$$u = \bar{u} + A\sin(m\varphi - 2\pi f_0 t), \quad v = \bar{v} + A\sin(m\varphi - 2\pi f_0 t), \quad w = \bar{w} + A\sin(m\varphi - 2\pi f_0 t), \quad (15)$$

where A is the amplitude of disturbance, m is the mode number, φ is the azimuthal angle and f_0 the excitation frequency. The amplitude of the disturbance is 1% of the maximum value of the streamwise velocity. The non-dimensional frequency (Strouhal number) of the unsteady disturbance is chosen to be $f_0 = 0.3$, which is the most unstable mode leading to the jet-preferred mode of instability of round jets (Gutmark and Ho, 1983; Hussain and Zaman, 1981). Two helical disturbances of $m = 1$ and $m = -1$ were superimposed on the temporal disturbance (Uchiyama, 2004).

4. Computational details

The input parameters in the simulations were given in their non-dimensional form, estimated from the fluids properties of diesel injection into compressed air at 15 MPa and 300 K (Perry and Green, 1998). Using the reference quantities defined in Section 2, the non-dimensional input parameters used are: Mach number $Ma = 0.4$, Reynolds number $Re = 2000$, Prandtl number $Pr = 0.76$, Schmidt number $Sc = 0.76$ (defined as $Sc = \mu_g^*/\rho_g^* D_g^*$), Weber number $We = 240$, ratio of specific heats $\gamma = 1.64$ A, and swirl number $S = 0.3$ with the swirling motion specified in the anti-clockwise direction at the jet nozzle exit. The dynamic gas viscosity is chosen to be temperature-dependent according to a power-law of the form $\mu_g = \mu_a (T/T_a)^{0.67}$ while the gas density is constant at the inflow. The non-dimensional width of the annular sheet is 0.35 while the thickness of the liquid sheet is 0.2 and it is located in the middle of the annulus. The simulated conditions correspond to diesel injection into compressed air at approximately 15 MPa and 300 K. At these conditions (Perry and Green, 1998), the gas density, dynamic viscosity and mass diffusivity are $\rho_g^* = 174\ \mathrm{kg/m^3}$, $\mu_g^* = 0.22 \times 10^{-4}$ kg/ms and $D_g^* = 1.66 \times 10^{-7}\ \mathrm{m^2/s}$, while the diesel fuel properties are: density $\rho_l^* = 840\ \mathrm{kg/m^3}$, kinematic viscosity $\mu_l^* = 3.0 \times 10^{-6}\ \mathrm{m^2/s}$ and surface tension $\sigma^* = 0.025$ N/m (the liquid properties are assumed to be constant). The dimensional injection velocity is 133.5 m/s. The dimensional inner and outer radii of the annular jet and liquid sheet, as indicated in Fig. 2 are

$$R^*_{o(jet)} = 1.35 \times 10^{-3}\ \mathrm{mm}; \quad R^*_{o(sheet)} = 1.20 \times 10^{-3}\ \mathrm{mm};$$
$$R_{i(sheet)} = 0.80 \times 10^{-3}\ \mathrm{mm}; \quad R^*_{i(jet)} = 0.65 \times 10^{-3}\ \mathrm{mm}.$$

The excessive computational cost needed to perform complex two-phase DNS, limits the computation to regions close to the jet

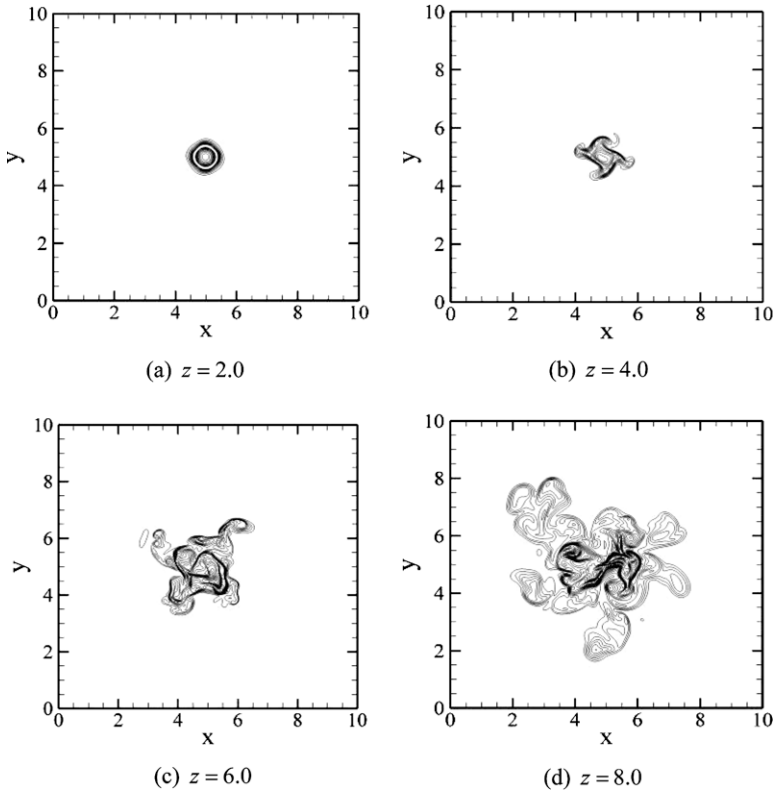

Fig. 4. Instantaneous liquid volume fraction contours in various streamwise planes at $t = 30.0$.

nozzle exit. The dimensions of the computational box used are $L_x = L_y = L_z = 10$. The grid system is of $512 \times 512 \times 512$ nodes with a uniform distribution in each direction. The grid determines the scales that are resolved while the resolution must be sufficient to capture the smallest scales. The Kolmogorov length scale is commonly quoted as the smallest scale that needs to be resolved in DNS-type simulations and can be defined as (Freitag and Klein, 2005) $\eta_K^* = L_{ref}^*/Re_t^{3/4}$, where L_{ref}^* is the dimensional reference length scale and Re_t is the turbulent Reynolds number based on the magnitude of velocity fluctuations. The L_{ref}^* corresponding to the nominal Reynolds and Mach numbers is around 2 μm for the simulations performed. Based on the non-dimensional input parameters and the velocity fluctuations observed in the flow fields, the Kolmogorov length scale η_K^* can be estimated to be around 0.3 μm with significant spatial variations, while the grid spacing η_{grid}^* is around 0.04 μm. However, the η_K^* estimated here might not be a good criterion to assess the quality of the simulation because of the laminar to transitional nature rather than fully turbulent nature of the flow. The physical scales of the problem corresponding to the non-dimensional parameters used are very small. However, tests showed that changing the Mach number from 0.4 to 0.05 did not lead to appreciable changes in the solution, indicating that the DNS results may be applicable to physical problems that are ten times larger than that indicated by the L_{ref}^*. The scaled-up physical scales correspond to those of micro-diesel injector nozzles (Baik et al., 2003) and microelectromechanical nozzles (Wang and Li, 2004). Although scaling to larger configurations can be approximate or even distorted, DNS results of this type can be used to gain better insights into practical problems. Under this perspective the results presented in this study are considered to be useful for understanding fuel injection processes in practical applications.

Parallel computation has been performed, under the MPI environment, on an IBM pSeries 690 Turbo Supercomputer HPCx utilising 512 processors. The 3D parallel DNS code used in this study was developed from the 3D parallel DNS code for gas jets (Jiang et al., 2007; Jiang and Luo, 2003) based on the gas–liquid two-phase flow formulation used in axisymmetric and planar simulations (Siamas et al., 2008a; Siamas and Jiang, 2007; Jiang and Siamas, 2007). Grid and time step dependence tests were also performed by doubling the grid points in one direction (tests by doubling the grid points in all directions proved to be too costly to perform) and halving the time step, which did not show appreciable changes in the results. The results presented are therefore considered to be of adequate resolution and are discussed in terms of the instantaneous and time-averaged flow properties.

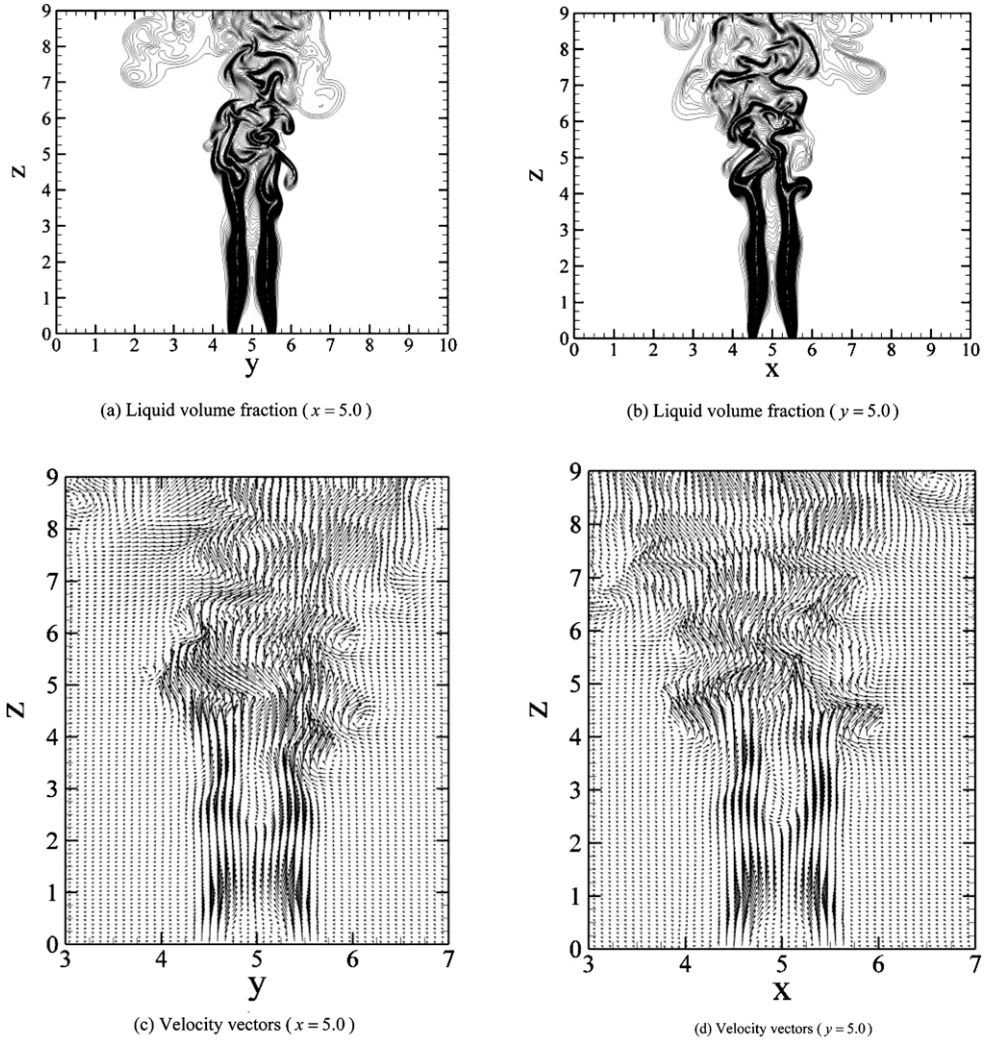

Fig. 5. Instantaneous liquid volume fraction contours and velocity vectors in $x = 5.0$ and $y = 5.0$ planes at $t = 30.0$.

5. Results and discussion

5.1. Instantaneous flow properties

Fig. 3 shows the instantaneous isosurfaces of enstrophy $\Omega = (\omega_x^2 + \omega_y^2 + \omega_z^2)/2$, liquid volume fraction Φ and vorticity components at $t = 30.0$. The individual vorticity components are defined as $\omega_x = \partial w/\partial y - \partial v/\partial z$, $\omega_y = \partial u/\partial z - \partial w/\partial x$ and $\omega_z = \partial v/\partial x - \partial u/\partial y$, respectively. From Fig. 3 it is evident that the dispersion of the liquid is dominated by vortical structures formed at the downstream locations. It is noticed that no significant vortices are developed at the upstream locations while the downstream vortex formation is a consequence of the spatial development of the flow due to the growth of the Kelvin–Helmholtz instability. In a 3D configuration, streamwise vorticity is generated by the 3D vortex stretching and interaction, a feature absent in idealised axisymmetric and planar configurations (Siamas et al., 2008a; Siamas and Jiang, 2007; Jiang and Siamas, 2007). The presence of both streamwise and cross-streamwise vorticity affects the liquid behaviour, as shown in Fig. 3b, with the liquid showing increasing spatial dispersion as the flow progresses from upstream to further downstream locations. The swirling mechanism causes the liquid surface to form a conical shape while the liquid overall dispersion is significantly greater compared to its corresponding non-swirling case (Siamas et al., 2008b). Fig. 3c and d shows the instantaneous isosurfaces of the x-vorticity and y-vorticity, respectively. It is noticed that both negative and positive vorticity is present, indicating the formation of complex vortices in the flow field. Negative and positive streamwise vorticity is also evident in Fig. 3e which shows the instantaneous isosurfaces of z-vorticity. This is due to the spatial development of the flow, which is more clearly shown in Fig. 3f which shows slices of the contours of the z-vorticity at three different streamwise locations, starting from $z = 2.0$ and progressing downstream to $z = 4.0$ and $z = 8.0$. Particularly at $z = 4.0$ and $z = 8.0$ complex vortical structures are formed, due to the spatial development of the jet and the growth of the instability.

To further elucidate the liquid distribution, Fig. 4 shows the instantaneous liquid volume fraction contours in various streamwise planes. At $z = 2.0$ a rather circular undistorted distribution is observed since the instability is not developed at this particular location. Further downstream the instantaneous spatial liquid dispersion shows complex helical patterns. The liquid distribution grows in the cross-streamwise directions as the flow progresses downstream, as shown in Fig. 4b–d, indicating larger spreading. The asymmetry observed in the downstream liquid dispersion is due to the two flapping modes (that are not symmetric in the azimuthal direction) applied at the nozzle exit, which triggers the flow instability and breaks the flow symmetry at downstream locations.

Fig. 5 shows the instantaneous liquid volume fraction contours and velocity vector maps in $x = 5.0$ and $y = 5.0$ planes at $t = 30.0$. Consistent with the observation in Fig. 3b the liquid dispersion is increased at downstream locations. The annular liquid column is broken into disorganised asymmetrical patterns which expand in both x- and y-directions. Streamwise vorticity, in conjunction with the inlet flapping modes, breaks the symmetry, as also occurred in the non-swirling case (Siamas et al., 2008b), while the swirling case reported herein shows larger liquid dispersion compared to the non-swirling case. The 3D swirling case also shows much larger spreading than the idealised axisymmetric and planar simulations (Siamas et al., 2008a; Siamas and Jiang, 2007) due to the 3D vortex stretching and interaction. In Fig. 5a and b, no significant liquid dispersion is observed from $z = 0$ to $z = 4.0$ since the Kelvin–Helmholtz instability is not developed and thus the annular liquid

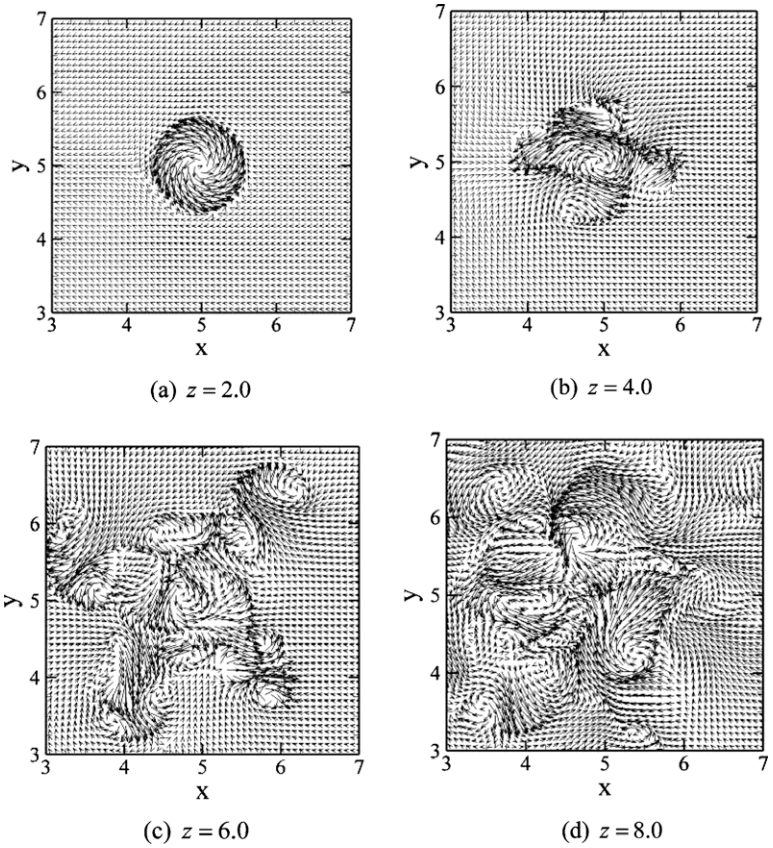

Fig. 6. Instantaneous velocity vector maps in various streamwise planes at $t = 30.0$.

column stays relatively unaltered. The liquid dispersion tendencies observed herein are in good agreement with the experimental observations of Ramamurthi and Tharakan (1998) who also noticed disorganised asymmetrical liquid patterns at further downstream locations. The annular jet develops an empty envelope adjacent to the jet nozzle exit as shown in Fig. 5a and b. This can be due to the presence of a geometrical recirculation zone (GRZ) which is formed adjacent to the nozzle exit (Siamas et al., 2008a; Sheen et al., 1996), a common feature of annular jet flows. Additional analysis of the recirculation zones is presented further on. From the velocity vector maps, shown in Fig. 5c and d, it is clear that the flow develops significant vortical structures after $z = 4.0$

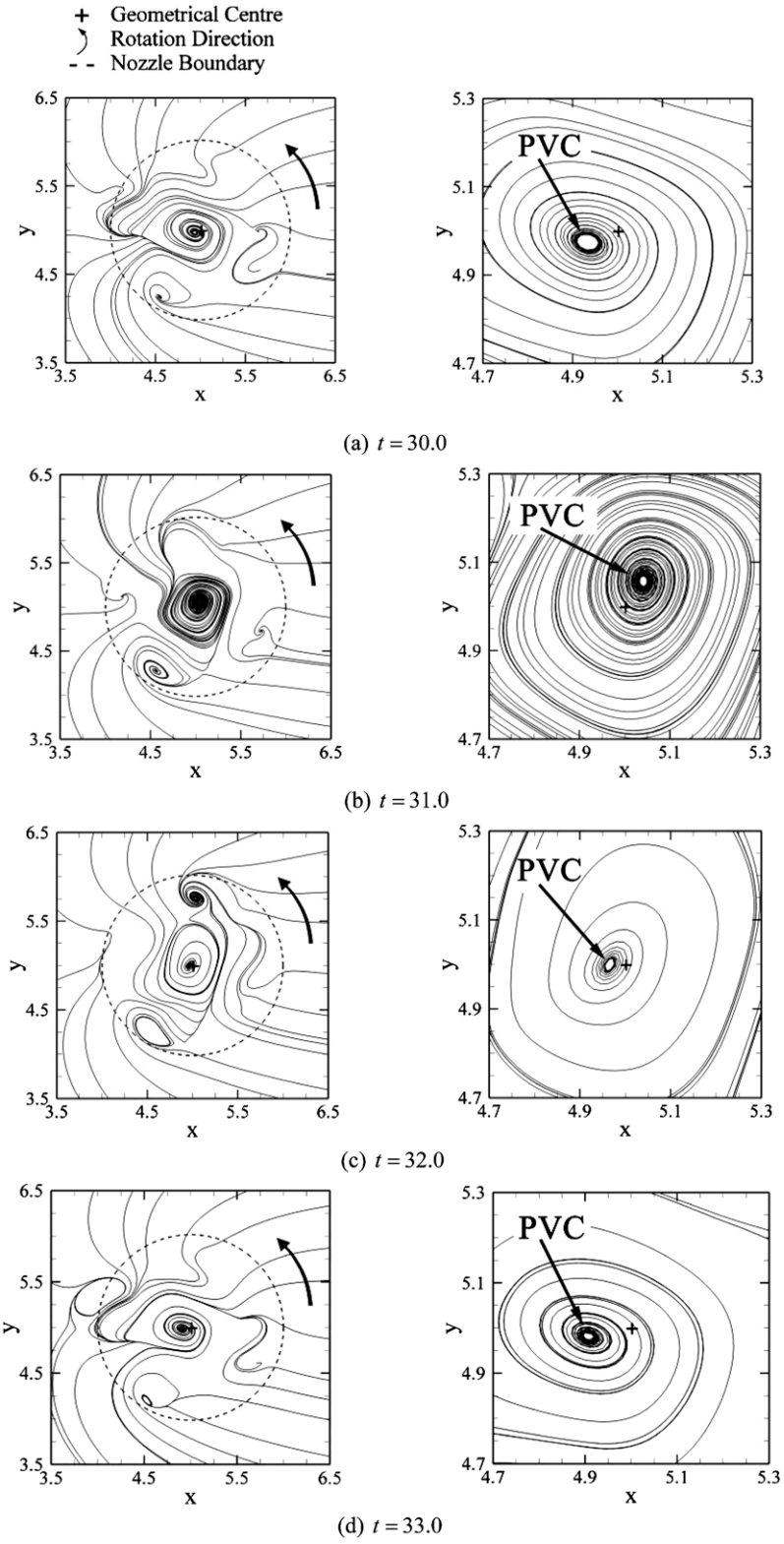

Fig. 7. Instantaneous streamtraces in $z = 4.0$ plane at different time instants.

in the streamwise direction, which are highly inhomogeneous with large spatial changes. After $z = 7.0$ the flow field appears to be more uniform where large-scale vortical structures are less obvious. This indicates that the large-scale structures might have broken down into smaller scales at the downstream.

The instantaneous velocity vector maps in various streamwise planes at $t = 30.0$ are shown in Fig. 6. For clarity reasons the vector plots shown are for a limited number of grid points which is significantly less than the total number of grid points. At $z = 2.0$, the swirling of the jet flow, which is a motion that is not self-sustaining, can be clearly seen. Further downstream the flow field shows complex structures due to the development of the instability which is triggered by the small external perturbation applied at the inlet. The instability development causes the flow structures to become more complex with less compactness, as shown in Fig. 6c and d, due to the collapsing of the large-scale structures to smaller ones. Compared with the rather compact flow structures observed in the non-swirling case (Siamas et al., 2008b), the results here indicate that the swirling motion enhances the instability and thus promotes vorticity. At the downstream location $z = 8.0$ the flow is more vortical but also more homogeneous compared to the other stream wise planes.

Instantaneous streamtraces in $z = 4.0$ plane at different time instants are presented in Fig. 7. The number and positioning of the streamtraces has been kept the same in all sub-figures for a consistent comparison. In Fig. 7, an inner self-rotating structure very close to the jet nozzle geometrical centre can be observed, which is known as the precessing vortex core (PVC) (Gupta et al., 1984). It is clear that the PVC changes position with time, showing a dynamic nature. The PVC not only rotates around its own axis but also rotates around the nozzle axis of symmetry. The PVC rotation direction is the same as the swirl direction indicated by the curved arrow in Fig. 7. It is known that the PVC can only develop in swirling jets but its exact mechanisms and the factors affecting its presence are still unclear (Syred, 2006; Lucca-Negro and O'Doherty, 2001). Garcia-Villalba and Frohlich (2006) showed that the PVC in single-phase flows is mainly associated with high swirl numbers ($S > 0.55$) and they did not observe a PVC in low swirl number case studies. This was noticed for swirling single-phase round jets (Syred, 2006; Gupta et al., 1984). Herein the swirl number is equal to 0.3 and a PVC development is observed as shown in Fig. 7. This is likely associated with the annular configuration of the jet and the gas–liquid two-phase flow investigated. It was experimentally shown (Al-Abdeli and Masri, 2003, 2004) that the PVC development in annular jet configurations is greatly affected by other inlet parameters, apart from the swirl number, and thus the swirl number alone is not a sufficient criterion for the PVC development. In a gas–liquid two-phase flow system, the large liquid-to-gas density ratio increases the azimuthal momentum flux (compared with a single-phase gas jet). Consequently, PVC may develop at a smaller swirl number, which was defined based on azimuthal velocity only. The amplitude of the PVC motion is quite small compared to the jet diameter, consistent with experimental observations, in which small motions of the PVC were normally observed (Fick et al., 1997; Syred et al., 1997). The PVC could only extend its motion beyond half of the jet diameter in cases of extreme swirl (Gupta et al., 1984).

The instantaneous streamwise velocity profiles at the jet centreline at different time instants are shown in Fig. 8. A large peak, having a maximum at $z = 1.5$, is observed near the nozzle exit due to the merging of the circular sheet of the annular jet. The

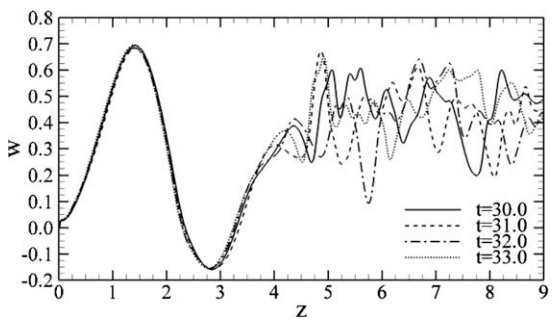

Fig. 8. Instantaneous streamwise velocity profiles at the jet centreline at different time instants.

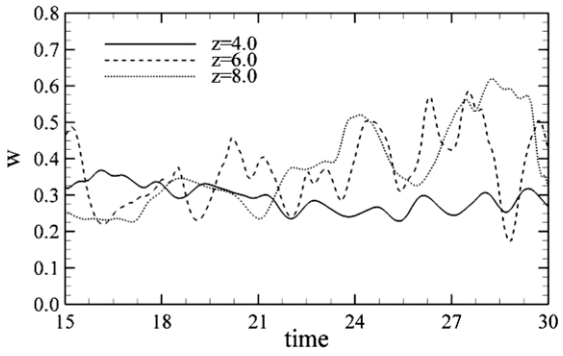

(a) Centreline velocity histories

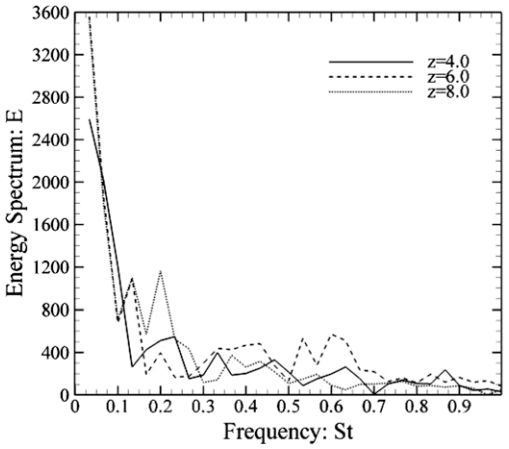

(b) Energy spectra from a Fourier transform

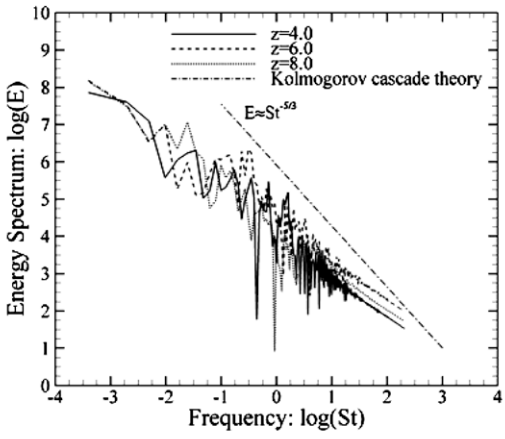

(c) Energy spectra in logarithmic scales

Fig. 9. Centreline velocity histories and their corresponding energy spectra.

streamwise velocity profiles are overlapping and have negative values between $z = 2.25$ and $z = 3.25$. This is associated with the development of a recirculation zone at this particular region. The positioning of this negative velocity zone (a recirculation zone) is further downstream and not adjacent to the nozzle exit, and thus it cannot be regarded as a GRZ. It is rather a central recirculation zone (CRZ) which is due to the swirling motion applied at the inlet (Syred, 2006). The velocity profiles at the downstream, and particularly after $z = 5.0$, show significant fluctuations indicating that the Kelvin–Helmholtz instability is established causing the flow field to become more vortical.

Fig. 9 shows, by means of time traces, the streamwise velocity histories at the jet centreline along with their corresponding energy spectra at three locations starting from $z = 4.0$ and progressing downstream to $z = 6.0$ and $z = 8.0$. It is noticed that at $z = 4.0$ the velocity fluctuations are relatively weak indicating a rather stable flow field in terms of vorticity. At $z = 6.0$ more significant velocity fluctuations are present, associated with the formation and convection of large-scale vortical structures which ultimately change the local velocity. Further downstream, at $z = 8.0$, the velocity fluctuations are slightly smoother compared to the ones at $z = 6.0$, indicating that the large-scale vortical structures might have collapsed to smaller ones. Fig. 9b shows the energy spectra from a Fourier analysis of the streamwise velocity histories, as shown in Fig. 9a, for the three downstream locations considered. Although a small external perturbation was applied at the inlet with frequency $St = 0.3$, non-zero dominant frequencies are not observed in Fig. 9b. This may be due to the complex dynamic nature of the two-phase flow field, and the fact that the flow has not been fully developed or the time interval examined is not sufficiently long enough. The small peaks and troughs observed in the energy distributions are due to the vortex interaction that occurs in the flow. The energy spectra are also plotted in logarithmic scales as shown in Fig. 9c. The important feature in Fig. 9c is the large energy fluctuations observed in downstream locations, indicating the transitional behaviour of the annular gas–liquid two-phase jet. In comparison with the non-swirling case (Siamas et al., 2008b) the addition of swirl results in a more energetic flow field and thus the vortical level of the flow is also increased. The transition to turbulence can be measured by the Kolmogorov cascade theory, e.g. Grinstein and DeVore (1996), which states a power-law correction between the energy and the frequency of the form $E \approx St^{-5/3}$. In Fig. 9c the Kolmogorov power-law is plotted together with the energy spectrum at the downstream locations under consideration. It is noticed that the annular jet behaviour does not closely follow the Kolmogorov cascade theory, indicating the laminar to transitional nature of the gas–liquid two-phase flow.

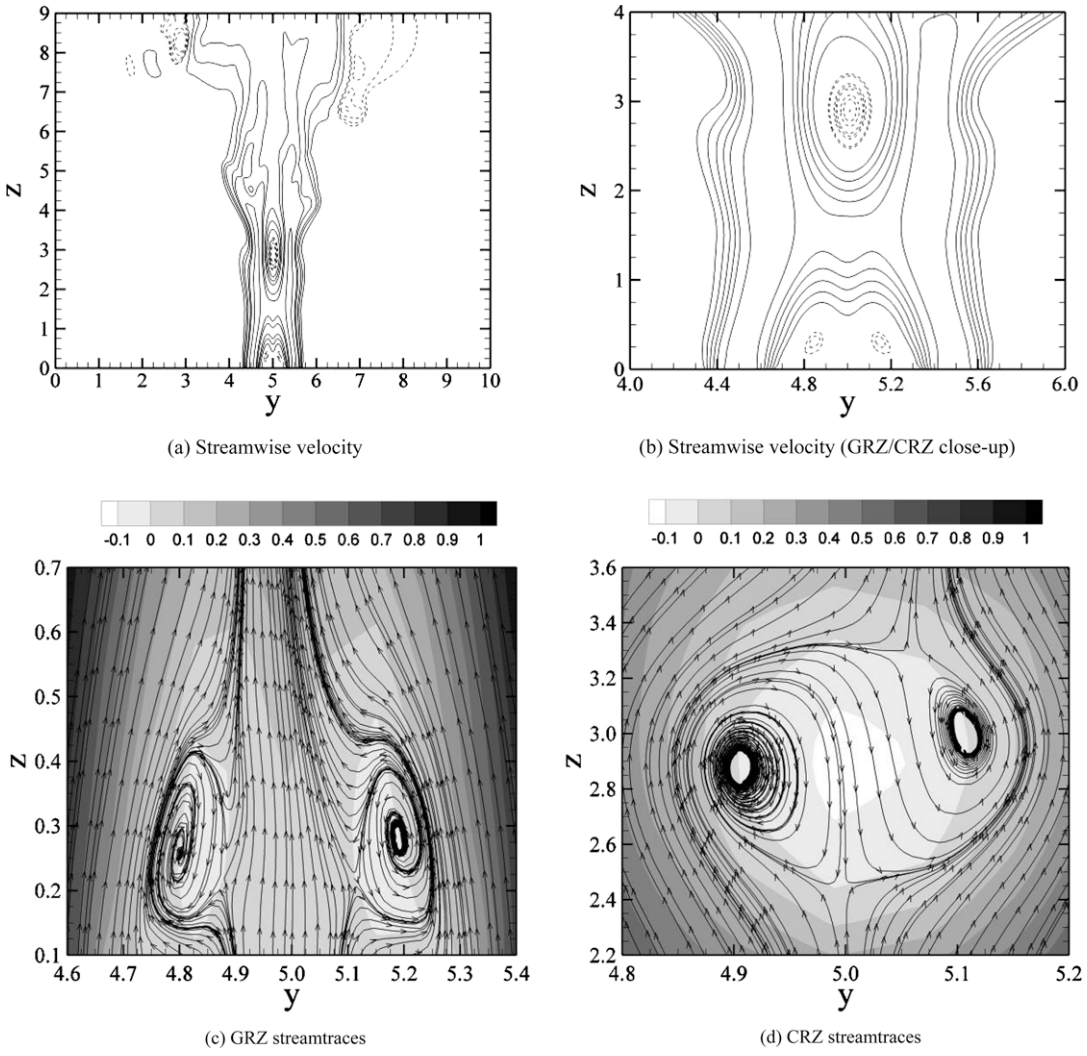

Fig. 10. Time-averaged streamwise velocity contours and streamtraces of the recirculation zones in $x = 5.0$ plane (solid line: positive; dashed line: negative).

5.2. Time-averaged flow properties

In an effort to further understand the flow physics and examine the recirculation characteristics, time-averaged results are also presented. The time interval used for the calculation of the averaging properties is between $t_1 = 23.3$ and $t_2 = 30.0$ after the flow has developed. Fig. 10a and b shows the time-averaged streamwise velocity contours in $x = 5.0$ plane. No vortical structures are observed since vortical structures are dynamic which are continuously convected downstream by the mean flow and therefore they would not appear in the averaged results. The flow shows no significant spreading until $z = 4.0$. After $z = 4.0$ the Kelvin–Helmholtz instability is established causing the jet to spread more in the cross-streamwise direction. The most important feature in Fig. 10a and b is the capturing of two recirculation zones: (1) a geometrical recirculation zone adjacent to the nozzle exit and (2) a central recirculation zone having its centre approximately at $z = 3.0$ and $y = 5.0$. The GRZ is a typical feature of annular jet flows due to the two concentric shear layers (Siamas et al., 2008a; Sheen et al., 1996). In this cross-section, the GRZ has two branches on both sides of the centreline. The CRZ is positioned in between $z = 2.2$ and $z = 3.4$ and it is purely due to the swirling mechanism.

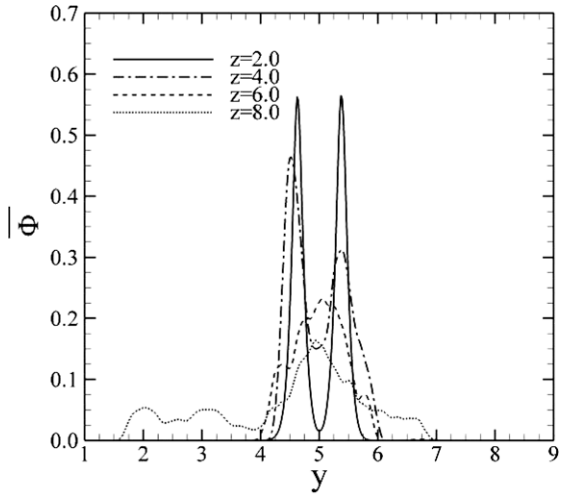

(a) Liquid volume fraction

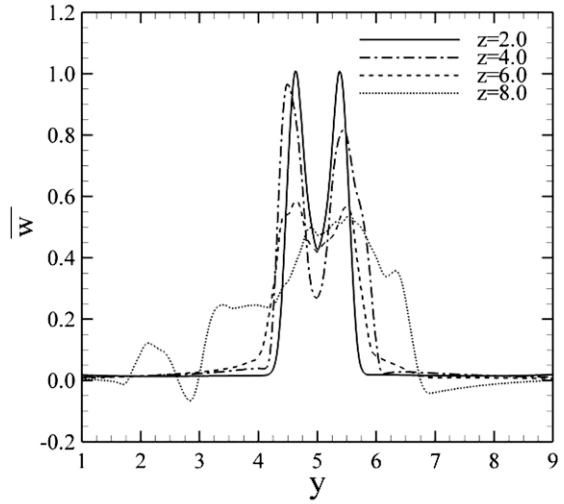

(b) Streamwise velocity

Fig. 11. Time-averaged liquid volume fraction and streamwise velocity profiles at different streamwise locations in $x = 5.0$ plane.

Our earlier results of non-swirling gas–liquid jet flows (Siamas et al., 2008b) showed that only the GRZ adjacent to the jet nozzle exit is evident. The DNS results shown here indicate that the swirling motion is responsible for the development of the CRZ, in support with the observations of Syred (2006), Lucca-Negro and O'Doherty (2001). The rotating patterns of both the GRZ and the CRZ are clearly shown in Fig. 10c and d, respectively. For better visualisation the streamtraces are plotted on top of the time-averaged streamwise velocity contours. The streamtraces are in support of the negative streamwise velocity present and they clearly show the recirculating behaviour of both the GRZ and the CRZ.

The time-averaged liquid volume fraction and streamwise velocity profiles in different streamwise locations in $x = 5.0$ are shown in Fig. 11a and b. The asymmetries observed at the downstream locations in both figures are due to the two asymmetric helical modes supplied at the inlet and possibly the insufficient time interval for the averaging. At $z = 2.0$ the liquid volume fraction profiles show two branches and a deep crest. This is due to the annular configuration of the jet. At further downstream locations the profiles show irregular asymmetrical distributions indicating that the annular jet column has collapsed somewhere between $z = 2.0$ and $z = 4.0$. The profiles show increasing cross-streamwise distributions with decreasing magnitudes as the flow progresses from upstream to further downstream locations. This is consistent with the observations in Fig. 3b indicating the "conical" distribution of the liquid from the inlet to the downstream. The time-averaged streamwise velocity profiles, as shown in Fig. 11b, are very similar to the liquid volume fraction profiles shown in Fig. 11a. Decreasing velocity magnitudes are observed at progressing downstream locations due to the mixing of the annular jet with its ambient quiescent environment. The complexity of the profiles, especially at $z = 8.0$, indicates that the flow is experiencing significant mixing with the ambient.

6. Conclusions

Direct numerical simulation of an annular gas–liquid two-phase swirling jet has been performed in this study. The code is parallelized, based on domain decomposition under the message passing interface environment. An Eulerian approach with mixed-fluid treatment has been utilised in the mathematical formulation. The governing equations are solved using highly accurate numerical schemes for time advancement and discretisation. The numerical procedures include an adapted volume of fluid method to account for the compressible gas phase while the surface tension effects are captured using a continuum surface force model. Helical perturbations are applied at the inflow to initiate the Kelvin–Helmholtz instability. The specification of swirl at the inlet is based on analytical conditions.

The results show that the flow is characterised by a geometrical recirculation zone adjacent to the jet nozzle exit due to the two concentric shear layers in the annular configuration. The swirling mechanism is responsible for the development of a central recirculation zone further downstream, a feature which is absent in annular gas–liquid non-swirling jet flow. Furthermore, the swirl applied at the inlet is responsible for the development of a precessing vortex core which changes position with time. The flow field is more energetic downstream, while its vorticity distribution becomes more homogeneous at further downstream locations. The swirling motion promotes the instability and thus the liquid spatial dispersion, in comparison to non-swirling cases. Analysis of the energy spectrum shows that the jet has no obvious tendency of transition to turbulence.

Direct numerical simulations of swirling gas–liquid two-phase flow systems can contribute towards full understanding of the

complex mechanisms behind liquid breakup and atomisation. The excessive amount of computer resources needed to perform such computations is a major drawback. Therefore the simulations had to be restricted to regions very close to the jet nozzle exit. The results presented herein are considered to be useful for understanding injection processes in microelectromechanical nozzles and can be helpful in the design of micro-scale injector systems. Extending the simulation to much larger domains in the near future would allow details of liquid disintegration and droplet formation to be captured and analyzed, allowing a more relevant and rigorous study of liquid breakup and atomisation.

Acknowledgement

This work was supported by the UK Turbulence Consortium (UKTC) under EPSRC Grant No. EP/D044073/1, which has provided the computing resources on the UK's national high-performance computing service HPCx.

References

Adzic, M., Carvalho, I.S., Heitor, M.V., 2001. Visualisation of the disintegration of an annular liquid sheet in a coaxial airblast injector at low atomising air velocities. Opt. Diagnost. Eng. 5, 27–38.

Al-Abdeli, Y.M., Masri, A.R., 2003. Recirculation and flowfield regimes of unconfined non-reacting flows. Exp. Therm. Fluid Sci. 27, 655–665.

Al-Abdeli, Y.M., Masri, A.R., 2004. Precession and recirculation in turbulent swirling isothermal jets. Combust. Sci. Tech. 176, 645–665.

Baik, S., Blanchard, J.P., Corradini, M.L., 2003. Development of micro-diesel injector nozzles via electromechanical systems technology and effects on spray characteristics. J. Eng. Gas Turbines Power 125, 343–427.

Banerjee, S., Lakehal, D., Fulgosi, M., 2004. Surface divergence models for scalar exchange between turbulent streams. Int. J. Multiphase Flow 30, 963–977.

Brackbill, J.U., Kothe, D.B., Zemach, C., 1992. A continuum method for modelling surface tension. J. Comput. Phys. 100, 335–354.

Chuech, S.G., 1993. Numerical simulation of nonswirling and swirling annular liquid jets. AIAA J. 31, 1022–1027.

Crowe, C.T., 2006. Multiphase Flow Handbook. Taylor & Francis, USA.

Del Taglia, C., Blum, L., Gass, J., Ventikos, Y., Poulikakos, D., 2004. Numerical and experimental investigation of an annular jet flow with large blockage. J. Fluid Eng. 126, 375–384.

Fick, W., Griffiths, A.J., O'Doherty, T., 1997. Visualisation of the precessing vortex core in an unconfined swirling flow. Opt. Diagnost. Eng. 2, 19–31.

Freitag, M., Klein, M., 2005. Direct numerical simulation of a recirculating, swirling flow. Flow Turbul. Combust. 75, 51–66.

Fulgosi, M., Lakehal, D., Banerjee, S., DeAngelis, V., 2003. Direct numerical simulation of turbulence in a sheared air–water flow with a deformable interface. J. Fluid Mech. 482, 319–345.

Garcia-Villalba, M., Frohlich, J., 2006. LES of a free annular swirling jet – dependence of coherent structures on a pilot jet and the level of swirl. Int. J. Heat Fluid Flow 27, 911–923.

Garcia-Villalba, M., Frohlich, J., Rodi, W., 2006. Identification and analysis of coherent structures in the near field of a turbulent unconfined annular swirling jet using large eddy simulation. Phys. Fluid 18, 055103/1–055103/17.

Gorokhovski, M., Hermann, M., 2008. Modeling primary atomization. Annu. Rev. Fluid Mech 40, 343–366.

Grinstein, F.F., DeVore, C.R., 1996. Dynamics of coherent structures and transition to turbulence in free square jets. Phys. Fluids 8, 1237–1251.

Gueyffier, D., Li, J., Nadim, A., Scardovelli, R., Zaleski, S., 1999. Volume-of-fluid interface tracking with smoothed surface stress methods for three-dimensional flows. J. Comput. Phys. 152, 423–456.

Gupta, K., Lilley, D.G., Syred, N., 1984. Swirl Flows. Abacus Press, Kent.

Gutmark, E., Ho, C.-M., 1983. Preferred modes and the spreading rates of jets. Phys. Fluids 26, 2932–2938.

Hirt, C.W., Nichols, B.D., 1981. Volume of fluid (VOF) method for the dynamics of free boundaries. J. Comput. Phys. 39, 201–225.

Hübner, A.W., Tummers, M.J., Hanjalic, K., van der Meer, Th.H., 2003. Experiments on a rotating-pipe swirl burner. Exp. Ther. Fluid Sci. 27, 481–489.

Hussain, A.K.M.F., Zaman, K.B.M.Q., 1981. The preferred mode of the axisymmetric jet. J. Fluid Mech. 110, 39–71.

Ibrahim, E.A., McKinney, T.R., 2006. Injection characteristics of non-swirling and swirling annular liquid sheets. Proc. Inst. Mech. Eng. Part C: J. Mech. Eng. Sci. 220, 203–214.

Jakirlic, S., Hanjalic, K., Tropea, C., 2002. Modeling rotating and swirling turbulent flows: a perpetual challenge. AIAA J. 40, 1984–1996.

Jiang, X., Luo, K.H., 2000. Direct numerical simulation of the puffing phenomenon of an axisymmetric thermal plume. Theor. Comput. Fluid Dyn. 14, 55–74.

Jiang, X., Luo, K.H., 2003. Dynamics and structure of transitional buoyant jet diffusion flames with sidewall effects. Combust. Flame 133, 29–45.

Jiang, X., Siamas, G.A., 2007. Direct computation of an annular liquid jet. J. Algo. Comput. Tech. 1, 103–125.

Jiang, X., Zhao, H., Luo, K.H., 2007. Direct computation of perturbed impinging hot jets. Comput. Fluid 36, 259–272.

Jiang, X., Siamas, G.A., Wrobel, L.C., 2008. Analytical equilibrium swirling inflow conditions for computational fluid dynamics. AIAA J. 46, 1015–1019.

Klein, M., 2005. Direct numerical simulation of a spatially developing water sheet at moderate Reynolds number. Int. J. Heat Fluid Flow 26, 722–731.

Kollmann, W., Ooi, A.S.H., Chong, M.S., Soria, J., 2001. Direct numerical simulations of vortex breakdown in swirling jets. J. Turbulence 2. Art. No. N5.

Lele, S.K., 1992. Compact finite-difference schemes with spectral-like resolution. J. Comput. Phys. 103, 16–42.

Liao, Y., Jeng, S.M., Jog, M.A., Benjamin, M.A., 2000. Instability of an annular liquid sheet surrounded by swirling airstreams. AIAA J. 38, 453–460.

Lombardi, P., DeAngelis, V., Banerjee, S., 1996. Direct numerical simulation of near-interface turbulence in coupled gas–liquid flow. Phys. Fluid 8, 1643–1665.

Lucca-Negro, O., O'Doherty, T., 2001. Vortex breakdown: a review. Prog. Energy Combust. Sci. 27, 431–481.

Perry, R.H., Green, D.W., 1998. Perry's Chemical Engineers' Handbook. McGraw-Hill, Singapore.

Pierce, CD., Moin, P., 1998. Method for generating equilibrium swirling inflow conditions. AIAA J. 36, 1325–1327.

Ramamurthi, K., Tharakan, T.J., 1998. Flow transition in swirled liquid sheets. AIAA J. 36.

Ruith, M.R., Meiburg, E., 2002. Direct numerical simulation of spatially developing, three-dimensional swirling jets. J. Turbul. 3, N65.

Sheen, H.J., Chen, W.J., Jeng, S.Y., 1996. Recirculation zones of unconfined and confined annular swirling jets. AIAA J. 34, 572–579.

Siamas, G.A., Jiang, X., 2007. Direct numerical simulation of a liquid sheet in a compressible gas stream in axisymmetric and planar configurations. Theor. Comput. Fluid Dyn. 21, 447–471.

Siamas, G.A., Jiang, X., Wrobel, L.C., 2008a. A numerical study of an annular liquid jet in a compressible gas medium. Int. J. Multiph. Flow 34, 393–407.

Siamas, G.A, Jiang, X., Wrobel, L.C., 2008b. Spatial DNS of a perturbed compressible annular two-phase jet. In: Proceedings of the Seventh International ERCOFTAC Symposium on Engineering Modelling and Measurements (ETMM-7), Limassol, Cyprus, pp. 156-161.

Sommerfeld, M., Qiu, H.-H., 1991. Detailed measurements in a swirling paniculate two-phase flow by a phase-Doppler anemometer. Int. J. Heat Fluid Flow 12, 20–28.

Syred, N., 2006. A review of oscillation mechanisms and the role of the precessing vortex core (PVC) in swirl combustion systems. Prog. Energy Combust. Sci. 32, 93–161.

Syred, N., Fick, W., O'Doherty, T., Griffiths, A.J., 1997. The effect of the precessing vortex core on combustion in a swirl burner. Combust. Sci. Tech. 125, 139–157.

Thompson, K.W., 1987. Time dependent boundary conditions for hyperbolic systems. J. Comput. Phys. 68, 1–24.

Uchiyama, T., 2004. Three-dimensional vortex simulation of bubble dispersion in excited round jet. Chem. Eng. Sci. 59, 1403–1413.

Vanierschot, M., van den Bulck, E., 2007. Hysteresis in flow patterns in annular swirling jets. Exp. Thermal Fluid Sci. 31, 513–524.

Wang, M.R., Li, Z.X., 2004. Numerical simulations on performance of MEMS-based nozzles at moderate or low temperatures. Microfluid. Nanofluid. 1, 62–70.

Williamson, J.H., 1980. Low-storage Runge–Kutta schemes. J. Comput. Phys. 35, 1–24.

Wray, A.A., 1986. Very low storage time-advancement schemes, Internal Report, NASA-Ames Research Center, Moffett Field, California.